


## Article

# New Insights into the Effect of Ce Doping on the Catalytic Performance and Hydrothermal Stability of Cu-USY Zeolite Catalysts for the Selective Catalytic Reduction of NO with NH<sub>3</sub>

Qi Sun <sup>1,2</sup>, Haipeng Yang <sup>3</sup>, Jie Wan <sup>1,3,\*</sup> , Wanru Hua <sup>2</sup>, Yanjun Liu <sup>1</sup>, Xiaoli Wang <sup>2</sup>, Chunxiao Shi <sup>4</sup>, Qingai Shi <sup>4</sup>, Gongde Wu <sup>1</sup> and Renxian Zhou <sup>3,\*</sup>

<sup>1</sup> Energy Research Institute, Nanjing Institute of Technology, Nanjing 211167, China; sunnnqi@163.com (Q.S.); yjliu@njit.edu.cn (Y.L.); wugongde@njit.edu.cn (G.W.)

<sup>2</sup> School of Environmental Engineering, Nanjing Institute of Technology, Nanjing 211167, China; hwrhua@163.com (W.H.); wangxiaoli212@njit.edu.cn (X.W.)

<sup>3</sup> Institute of Catalysis, Zhejiang University, Hangzhou 310028, China; syj86136926@163.com

<sup>4</sup> Zhejiang NHU Co., Ltd., Shaoxing 312500, China; s.chunxiao@cnhu.com (C.S.); s.qingai@cnhu.com (Q.S.)

\* Correspondence: jwan@njit.edu.cn (J.W.); zhounrenxian@zju.edu.cn (R.Z.)

**Abstract:** 5Cu-USY and Ce-doped 5Cu8Ce-USY zeolite catalysts were prepared by the conventional impregnation method. The obtained catalysts were subjected to the hydrothermal ageing process. The catalytic performance of the selective catalytic reduction of NO<sub>x</sub> with NH<sub>3</sub> (NH<sub>3</sub>-SCR) was evaluated on both fresh and aged catalysts. Physical/chemical characterizations such as X-ray diffraction (XRD), H<sub>2</sub> temperature-programmed reduction (H<sub>2</sub>-TPR), and X-ray photoelectron spectroscopy (XPS) were performed, along with detailed in situ diffuse reflectance infrared Fourier-transform spectroscopy (DRIFTS) experiments including CO adsorption, NH<sub>3</sub> adsorption, and NO + O<sub>2</sub> reactions. Results showed that, for the 5Cu-USY catalyst, hydrothermal ageing treatment could somehow improve the low-temperature SCR activity, but it also led to significant formation of unfavorable byproducts NO<sub>2</sub> and N<sub>2</sub>O. Such an activity change can be attributed to hydrothermal ageing inducing the migration of isolated Cu<sup>+</sup> species in the sodalite cavities towards the super cages of the USY zeolites. The increased content of Cu<sup>+</sup> species in the super cages was beneficial for the low-temperature activity improvement, but, at the same time, it also facilitated ammonia oxidation at high temperatures. Ce doping after hydrothermal ageing has a “double-edged sword” effect on the catalytic performance. First of all, Ce doping can inhibit Cu species migration by self-occupying the internal cage sites; thus, the catalytic performance of 5Cu8Ce-USY-700H remains stable after ageing. Secondly, Ce doping introduces a CuO<sub>x</sub>–CeO<sub>2</sub> strong interaction, which facilitates lattice oxygen mobility by forming more oxygen vacancies so as to increase the concentration of surface active oxygen. These changes, on the one hand, could help to promote further oxidative decomposition of nitrate/nitrite intermediates and improve the catalytic performance. But, on the other hand, it also causes the byproduct generation to become more severe.

**Keywords:** NH<sub>3</sub>-SCR; Cu-USY; Ceria doping; hydrothermal stability; DRIFTS



**Citation:** Sun, Q.; Yang, H.; Wan, J.; Hua, W.; Liu, Y.; Wang, X.; Shi, C.; Shi, Q.; Wu, G.; Zhou, R. New Insights into the Effect of Ce Doping on the Catalytic Performance and Hydrothermal Stability of Cu-USY Zeolite Catalysts for the Selective Catalytic Reduction of NO with NH<sub>3</sub>. *Catalysts* **2023**, *13*, 1485. <https://doi.org/10.3390/catal13121485>

Academic Editor: Leonarda Liotta

Received: 15 November 2023

Revised: 28 November 2023

Accepted: 29 November 2023

Published: 30 November 2023



**Copyright:** © 2023 by the authors. Licensee MDPI, Basel, Switzerland. This article is an open access article distributed under the terms and conditions of the Creative Commons Attribution (CC BY) license (<https://creativecommons.org/licenses/by/4.0/>).

## 1. Introduction

The booming development of modern transportation has brought great convenience to both daily life and industrial production, but the environmental pollution and human health hazards caused by vehicle exhaust have posed serious challenges to building a sustainable society. Diesel-engine-powered vehicles have attracted vast attention owing to their higher power and thermal efficiency [1]. However, nitrogen oxides (NO<sub>x</sub>) emitted from diesel engines are recognized as major culprits for photochemical smog, acid rain, and ozone layer depletion, as well as various diseases of the human respiratory, nervous,

and cardiovascular systems [2]. Among various denitrification ( $\text{deNO}_x$ ) techniques, selective catalytic reduction of  $\text{NO}_x$  with ammonia as reductant ( $\text{NH}_3$ -SCR) has been widely accepted and applied as the most practical approach for  $\text{NO}_x$  elimination regarding diesel engine exhaust [3]. Developing highly efficient novel catalysts is the key to pushing forward  $\text{NH}_3$ -SCR technology.  $\text{V}_2\text{O}_5$ - $\text{WO}_3$ - $\text{TiO}_2$  (VWTi) mixed oxides, known as the early generation of commercialized SCR catalysts, have been successfully employed in diesel engine vehicle  $\text{deNO}_x$  systems since the 1970s [4]. Unfortunately, with more stringent emission regulations, several challenges are raised against VWTi catalysts, such as inferior performance under lean combustion conditions, limited operation temperature windows, insufficient low-temperature activity, and poor thermal stability, as well as the biological toxicity of Vanadium species [5,6]; therefore, the urgent demand for developing novel SCR catalysts has drawn continuous interest in academia and industry.

Transitional-metal-doped zeolite catalysts have been extensively studied for the  $\text{NH}_3$ -SCR reaction during the past few decades [7,8]. Fe-based zeolite catalysts such as Fe-ZSM-5 were first proposed as promising for  $\text{NH}_3$ -SCR due to their wide operation temperature windows, especially at high temperature ranges [9]. However, such Fe-ZSM-5 catalysts generally present unsatisfactory low-temperature SCR activity below 250 °C, and the excessive oxidizing ability of Fe ions also causes the unfavorable  $\text{NH}_3$  oxidation problem [10]. Sequentially, Cu-based zeolites have been investigated as advantageous candidates for  $\text{NH}_3$ -SCR, i.e., Cu-ZSM-5, Cu-Beta, Cu-SAPO-34, Cu-USY, and Cu-SSZ-13. Cu-ZSM-5 zeolite catalysts are reported to exhibit high NO conversion rates, but their applications are prohibited by the poor hydrothermal stability of ZSM-5 due to gradual dealumination [11–13]. Cu-based small-pore zeolites with unique chabazite structures (especially Cu-SSZ-13) have demonstrated their excellent SCR activity and good hydrothermal stability and are currently the hot-topic catalysts attracting lots of attention [14]. However, the synthesizing process of the SSZ-13 zeolite requires using an expensive organic template (N,N,N-trimethyl-1-adamantammonium hydroxide, TMAOH), and its initial patents lie in the hands of certain industrial giants [15,16]. Hence, the high raw material cost and intellectual property issues of Cu-SSZ-13 zeolites remain inevitable challenges.

USY zeolites possess the advantages of excellent hydrothermal stability, a super large specific surface area, and a unique super cage structure. Ochońska et al. [17] reported that NO conversion over Cu-USY can exceed 50% at temperatures as low as 100 °C, attributable to the high concentration of  $\text{Cu}^+$  species with lower binding energy on the Cu-USY surface. Our previous studies regarding  $\text{NH}_3$ -SCR performance over various Cu-zeolites also revealed that Cu-USY shows a wider NO conversion temperature window (from 150 °C to 400 °C) along with good  $\text{N}_2$  selectivity. It was also reported that introducing Ce into Cu-USY with proper doping content could enhance oxygen mobility as well as increase the active  $\text{Cu}^+$  sites concentration, thus benefiting low-temperature SCR performance [18,19]. Additionally, the stability of the designed catalysts is quite important for assessing their practical application potential. For the SCR reaction, the exhaust gas of diesel engine vehicles can have temperatures as high as 700 °C and contains a large proportion of water vapor. Zeolite catalysts could easily deactivate due to serious dealumination, zeolite framework collapse, or sintering of active metal under high-temperature, humid working conditions [20]. Improving hydrothermal stability by Ce doping has been well examined in Ce-based mixed oxides such as  $\text{MnO}_x$ - $\text{CeO}_2$ , but it is still not well interpreted and needs further exploration regarding Ce-doped USY zeolite catalysts.

In the current work, Cu-USY and Ce-doped Cu-USY zeolite catalysts were synthesized via simple impregnation method. The obtained catalysts were subjected to high-temperature hydrothermal ageing and evaluated for  $\text{NH}_3$ -SCR catalytic performances. Detailed characterizations including XRD,  $\text{H}_2$ -TPR, CO DRIFTS, XPS, and in situ reaction DRIFTS were conducted. The scope of this work is to gain new insight into how Ce doping affects the hydrothermal stability of Cu-USY catalysts from the perspective of structure–activity evolution as well as the reaction process.

## 2. Results and Discussion

### 2.1. $\text{NH}_3$ -SCR Catalytic Activity

Figure 1 presents the overall  $\text{NH}_3$ -SCR performance of the obtained 5Cu-USY and 5Cu8Ce-USY catalysts before/after hydrothermal ageing. Figure 1a shows the NO conversion curves. For the fresh catalysts, Ce doping could clearly promote the  $\text{NH}_3$ -SCR catalytic activity of Cu-USY zeolite catalyst. The temperature at which NO conversion achieved 90% SCR activity was dramatically reduced to about 130 °C over the 5Cu8Ce-USY sample, and the operation temperature window width (the temperature ranges within which the NO conversion stays above 90%) was also significantly broadened compared to that of the 5Cu-USY sample. Table S1 shows the comparison of the  $\text{NH}_3$ -SCR activity of fresh catalysts in this work with those from other similar previous reports. Such an improving effect of Ce doping on the SCR catalytic performance of the fresh Cu-USY catalyst was reported in our previous study [18], and it was proposed that Ce doping could introduce strong interaction between  $\text{CuO}_x$  and  $\text{CeO}_2$ , which facilitates lattice oxygen mobility and enhances the redox ability. For the hydrothermal aged catalyst, it is quite interesting that the low-temperature SCR activity, as well as the operation temperature window, of the aged 5Cu-USY-700H sample was obviously improved compared to that of the fresh 5Cu-USY, while no significant improvement nor deterioration was observed over the 5Cu8Ce-USY-700H catalyst, demonstrating its good stability against hydrothermal ageing. The  $\text{NH}_3$  conversion curves shown in Figure 1b present similar trends consistent with the NO conversion curves, suggesting that  $\text{NH}_3$  consumption is mainly caused by NO reduction. Figure 1c,d show the monitored concentration of unfavorable byproducts  $\text{NO}_2$  and  $\text{N}_2\text{O}$ , respectively. A small amount of  $\text{NO}_2$  can be detected due to the partial oxidation of  $\text{NH}_3$  when the reaction temperature exceeds 350 °C. For  $\text{N}_2\text{O}$  formation, a typical “saddle-shaped” curve can be seen. According to previous reports [14],  $\text{N}_2\text{O}$  formation at low and high temperatures usually occurs via different mechanisms. At high temperatures, the reaction goes via the standard SCR routes [14], and  $\text{N}_2\text{O}$  is mainly formed because of unfavorable  $\text{NH}_3$  oxidation, while, at low temperatures, the reaction goes via the fast SCR route, while  $\text{N}_2\text{O}$  formation is contributed by the generation and decomposition of  $\text{NH}_4\text{NO}_3$ .  $\text{NH}_4\text{NO}_3$  was formed on the Cu sites via the Langmuir–Hinshelwood mechanism under the “ $\text{NH}_3 + \text{NO} + \text{O}_2$ ” condition, and its subsequent decomposition led to  $\text{N}_2\text{O}$  formation. Ce doping slightly increased  $\text{NO}_2$  and  $\text{N}_2\text{O}$  formation over fresh catalysts, possibly due to its well-known oxidizing ability. After hydrothermal ageing, a sharp increase in  $\text{NO}_2/\text{N}_2\text{O}$  generation could be seen over both 5Cu-USY and 5Cu8Ce-USY, suggesting that the catalysts’ selectivity towards harmless  $\text{N}_2$  was relatively deteriorated by hydrothermal ageing.

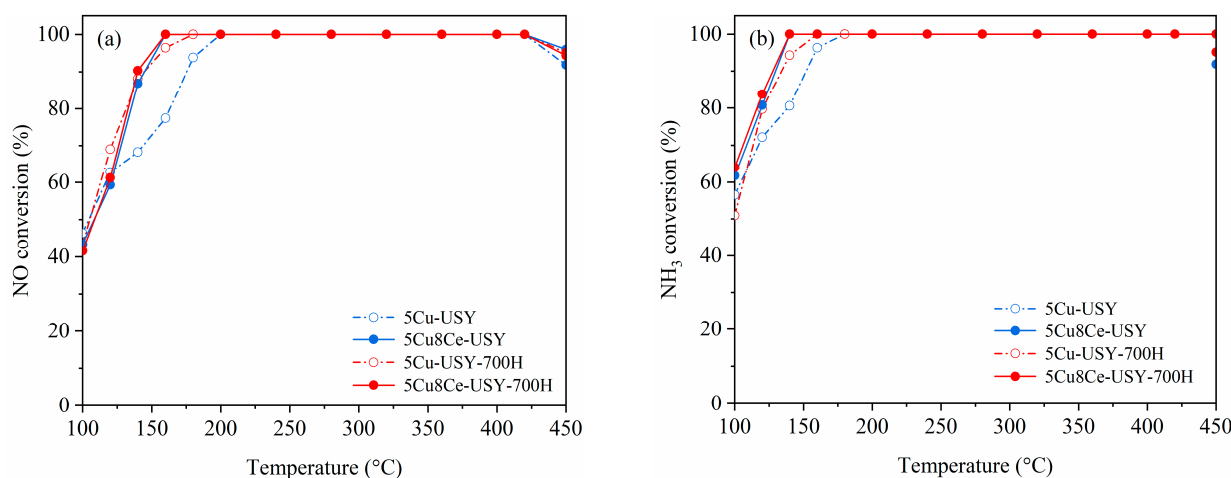
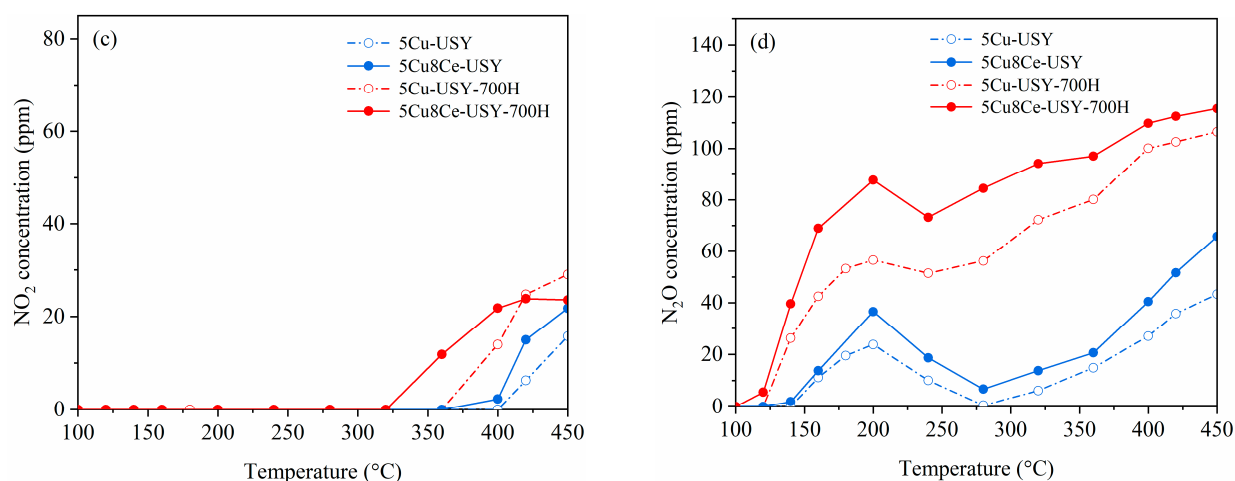


Figure 1. Cont.



**Figure 1.** NH<sub>3</sub>-SCR catalytic performances of 5Cu-USY and 5Cu8Ce-USY catalysts before/after hydrothermal ageing: NO conversion (a), NH<sub>3</sub> conversion rate (b), NO<sub>2</sub> concentration (c), and N<sub>2</sub>O concentration (d), reaction conditions: GHSV = 48,000 h<sup>−1</sup>, 500 ppm NO + 500 ppm NH<sub>3</sub>+5 vol.% O<sub>2</sub>, and Ar as balancing gas.

## 2.2. Crystalline Structure by XRD Analyses

The effect of hydrothermal ageing on the catalysts' crystalline structure was characterized by XRD analysis, and the obtained XRD patterns are shown in Figure 2. Distinctive diffraction peaks could be observed for all the samples around 6.3°, 10.3°, 12.0°, 15.8°, 18.9°, 20.6°, 23.9°, and 27.3°, which can be assigned to the (111), (220), (311), (331), (511), (440), (533), and (642) crystal planes of Y zeolites with a cubic structure (JCPDS 77-1549) [21]. The distinct peak shape with relatively strong intensity in the fresh 5Cu-USY and 5Cu8Ce-USY suggests that the zeolite structures with good crystallinity were not damaged by Cu/Ce impregnation. After hydrothermal ageing, these characteristic diffraction peaks could still be clearly observed in 5Cu-USY-700H and 5Cu8Ce-USY-700H samples, demonstrating that high-temperature hydrothermal ageing did not cause the zeolite framework to collapse. However, the peak's intensity was relatively decreased, which could be related to the weakened crystallinity caused by dealumination. The crystal sizes were also calculated using JADE software, and it can be seen that they only increased slightly after hydrothermal ageing. No characteristic diffraction peaks assigned to CuO, Cu<sub>2</sub>O, or CeO<sub>2</sub> species were observed in any of these XRD profiles, indicating that the CuO<sub>x</sub> and CeO<sub>2</sub> species were highly dispersed in the zeolite or formed agglomerated species with quite a small particle size that was beyond the XRD detection range.

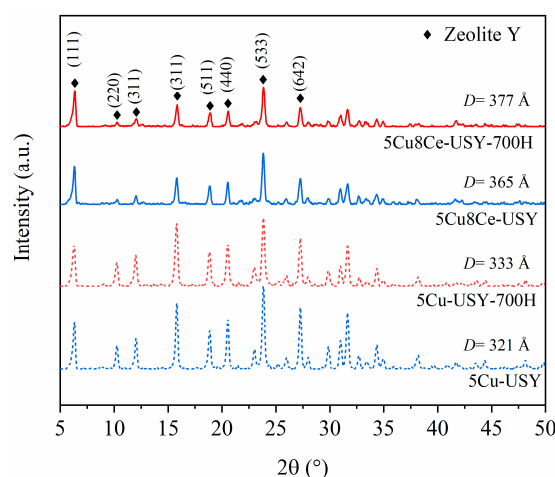


**Figure 2.** XRD patterns of 5Cu-USY and 5Cu8Ce-USY catalysts before/after hydrothermal ageing.

### 2.3. Redox Properties by $H_2$ -TPR Tests

The effect of hydrothermal ageing on the catalysts' redox properties was characterized by  $H_2$ -TPR tests, and the obtained  $H_2$ -TPR profiles are shown in Figure 3. Three major reduction peaks ( $\alpha$ ,  $\beta$ , and  $\gamma$ ) around 210 °C, 270 °C, and 340 °C could be verified over the 5Cu-USY catalyst, which can be assigned to the reduction of high valent cupric species [19,22,23]. According to previous studies, peak  $\alpha$  (210–215 °C) is generally attributed to the reduction of  $Cu^{2+}$  species located in the super cages of the USY framework; peak  $\beta$  (270–285 °C) can be assigned to the reduction in surface highly dispersed  $CuO_x$  species [22]; and peak  $\gamma$  (350–355 °C) represents the reduction in  $Cu^{2+}$  species located in the sodalite cavities of USY zeolites. For the Ce-doped 5Cu8Ce-USY catalyst, a new reduction peak ( $\delta$ ) appeared around 420 °C, which was related to the reduction in surface active oxygen of  $CeO_2$  [18]. The integrated peak areas and relative proportions of each peak were calculated and are shown in Table S2. After hydrothermal ageing, the intensity of peak  $\alpha$  was increased, while peak  $\gamma$ 's intensity weakened in the 5Cu-USY-700H sample. Such peak evolutions suggest that the  $Cu^{2+}$  species located in the sodalite cavities gradually migrate into the zeolite super cages during hydrothermal ageing. For the Ce-doped 5Cu8Ce-USY-700H sample, there was no significant change in the intensity of peaks  $\alpha$ ,  $\beta$ , and  $\gamma$ , indicating that Ce doping could well maintain the stability of  $Cu^{2+}$  species in the USY zeolites. Additionally, peak  $\delta$  in 5Cu8Ce-USY-700H drastically shifted to a lower temperature, which suggests that the reducibility of surface oxygen is improved due to enhanced interaction between  $CeO_2$  and  $CuO_x$  species during thermal ageing. This might be the main reason for the more severe  $NH_3$  oxidation, along with the deteriorated  $N_2$  selectivity, of 5Cu8Ce-USY-700H.

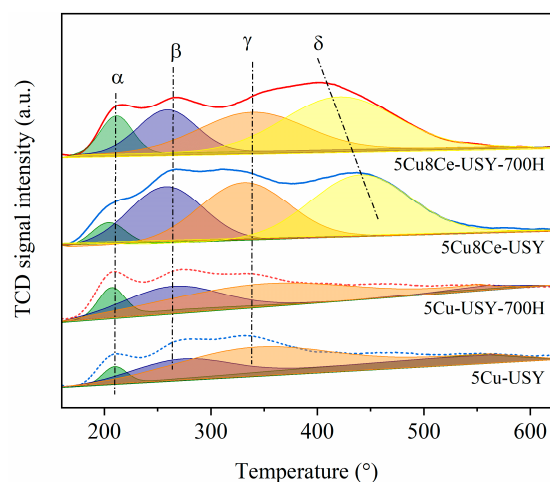


**Figure 3.**  $H_2$ -TPR profiles of 5Cu-USY and 5Cu8Ce-USY catalysts before/after hydrothermal ageing.

### 2.4. CO DRIFTS Analyses

The structural properties of Cu species were further investigated by CO DRIFTS analyses, and the obtained DRIFTS spectra are shown in Figure 4a. Two characteristic IR bands can be seen at  $2180\text{ cm}^{-1}$  and  $2153\text{ cm}^{-1}$ . According to Dang et al.'s reports [24], CO does not adsorb on  $Cu^{2+}$  sites at room temperature; thus, these IR bands are reasonably attributed to CO adsorption on  $Cu^+$  sites located within different environments in the USY zeolites. Based on previous reports [25,26], the IR band at  $2180\text{ cm}^{-1}$  can be attributed to  $Cu^+$  species located in the super cages of USY zeolites, which react with CO to form dicarbonyl species  $Cu^+-(CO)_2$ , while the IR band at  $2153\text{ cm}^{-1}$  corresponds to  $Cu^+$  species located in the sodalite cavities of USY zeolites, which form monocarbonyl species  $Cu^+-CO$  upon CO adsorption. The proportion of these two different  $Cu^+$  sites was semi-quantitatively determined by Gaussian fitting and peak area integration (shown in Figure 4b). Compared to the fresh 5Cu-USY catalyst, the  $Cu^+$  species located in the super cages increased quite

significantly after hydrothermal ageing, which once again proved that cupric species located in the sodalite cavities can gradually migrate into the zeolite super cages during hydrothermal ageing. However, for the 5Cu8Ce-USY-700H sample, the number of  $\text{Cu}^+$  species distributed and located in the sodalite cavities remained almost unchanged. This suggests that Ce doping could inhibit the migration of  $\text{Cu}^+$  species located in the sodalite cavities during hydrothermal ageing.

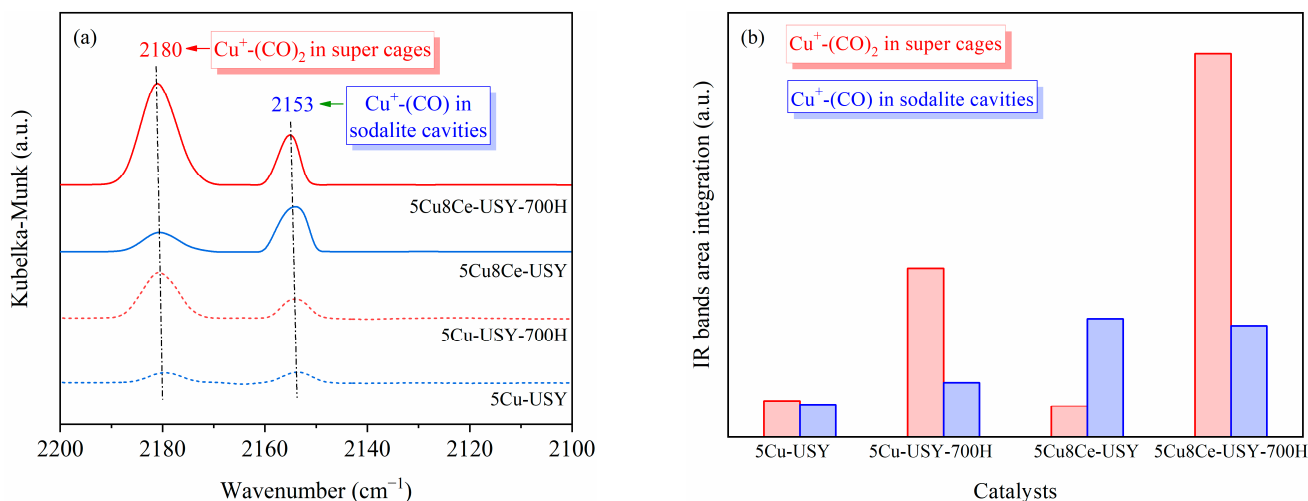


**Figure 4.** CO DRIFTS spectra (a) and peak area integration (b) of 5Cu-USY and 5Cu8Ce-USY catalysts before/after hydrothermal ageing.

### 2.5. Surface Chemistry by XPS

The surface chemical state changes before/after hydrothermal ageing were analyzed by XPS. The recorded spectra are shown in Figure 5. Figure 5a shows the Cu 2p spectra; all the catalysts exhibited typical Cu  $2p_{3/2}$  (binding energy around 933–935 eV) and Cu  $2p_{1/2}$  (binding energy around 953 eV) characteristic peaks. The Cu  $2p_{3/2}$  peaks can be further deconvoluted into two peaks, whereas the peak around 933.1 eV represents the  $\text{Cu}^+$  species, while the peak around 935.4 eV (with the shakeup satellite peak at 943.6 eV) is attributed to  $\text{Cu}^{2+}$  species (either in the form of isolated  $\text{Cu}^{2+}$  or CuO) [16,27,28]. Based on the quantitative results calculated in Table 1, we can see that, for the fresh 5Cu-USY catalyst, the surface Cu content was significantly lower than the theoretical value, indicating that a large proportion of Cu species entered the internal cage of the USY zeolite during preparation. On the other hand, the surface Cu content of 5Cu8Ce-USY was obviously higher than that of 5Cu-USY, while the surface Ce content was much lower than the theoretical values. This indicates that Ce doping could competitively occupy the site inside zeolite cages to partially prevent Cu species from entering zeolite cages. After hydrothermal ageing, the surface Cu content of 5Cu-USY-700H increased drastically. This phenomenon may be attributed to the unavoidable detachment of Cu species from the zeolite cages to form surface-dispersed CuOx species due to the thermal-induced driving force, causing an increase in the surface Cu content. Meanwhile, the  $\text{Cu}^+$  content on both 5Cu-USY and 5Cu8Ce-USY catalysts increased slightly, while the  $\text{Cu}^{2+}$  content decreased slightly.

Figure 5b shows the Ce 3d spectra. Eight characteristic peaks can be observed and divided as  $u$  series and  $v$  series, which originate from the split-orbit multiplex lines of  $3d_{3/2}$  and  $3d_{5/2}$ , respectively. Among these characteristic peaks,  $u$  (900.6–901.0 eV),  $u''$  (907.5–907.7 eV), and  $u'''$  (916.6–916.9 eV) can be assigned to  $\text{Ce}^{4+}$   $3d_{3/2}$  lines, while  $v$  (882.2–882.6 eV),  $v''$  (889.1–889.3 eV), and  $v'''$  (898.2–898.5 eV) can be assigned to  $\text{Ce}^{4+}$   $3d_{5/2}$  lines.  $\text{Ce}^{3+}$ -related lines are identified as  $u'$  (903.5–904.2 eV,  $\text{Ce}^{3+}$   $3d_{3/2}$ ) and  $v'$  (885.1–885.8 eV,  $\text{Ce}^{3+}$   $3d_{5/2}$ ) [29,30]. The ratio of  $\text{Ce}^{3+}$  in Ce was calculated via multi-peak fitting and peak area integration, as shown in Table 1. We can see that the  $\text{Ce}^{3+}/(\text{Ce}^{3+} + \text{Ce}^{4+})$  ratio increased after high-temperature hydrothermal ageing. Various

studies [31,32] have pointed out that the generation of  $\text{Ce}^{3+}$  requires the existence of oxygen vacancies. Therefore, such results provide further evidence that high-temperature hydrothermal ageing can facilitate oxygen vacancies formation, which can improve oxygen mobility by promoting the migration of lattice oxygen from the bulk phase to the catalyst's surface, thus being conducive to low-temperature SCR activity as well as the oxidation of NO to  $\text{NO}_2$ .

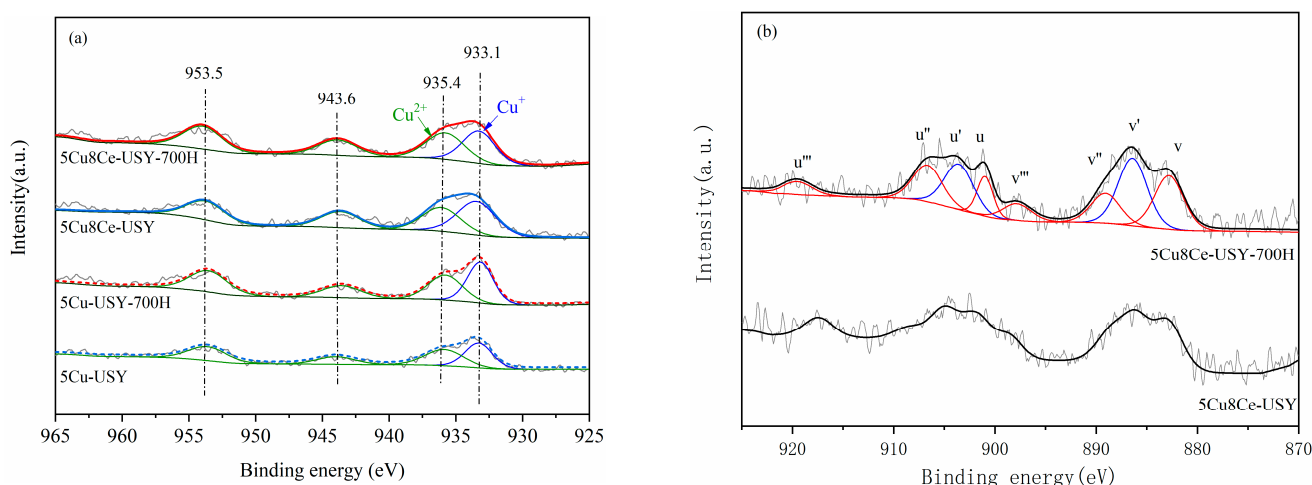


**Figure 5.** XPS spectra of 5Cu-USY and 5Cu8Ce-USY catalysts before/after hydrothermal ageing. Cu 2p (a) and Ce 3d (b).

**Table 1.** Surface element contents derived from XPS analyses.

Samples	Cu (wt.%)	Ce (wt.%)	Cu (%)		$\text{Ce}^{3+}$ in Ce (%)
			$\text{Cu}^+$	$\text{Cu}^{2+}$	
5Cu-USY	2.88	-	52.21	47.79	-
5Cu-USY-700H	4.17	-	55.39	44.61	-
5Cu8Ce-USY	4.20	2.62	46.14	53.86	22.07
5Cu8Ce-USY-700H	4.68	2.74	48.79	51.21	23.62

## 2.6. In Situ DRIFTS Characterizations

To acquire more insights into the effect of hydrothermal ageing on the reaction intermediates and structure–activity relationship for 5Cu-USY and 5Cu8Ce-USY catalysts, in situ DRIFTS characterizations were conducted under the “ $\text{NH}_3$  adsorption followed by  $\text{NO} + \text{O}_2$  reaction” process at 200 °C. The peak assignments based on the previous literature are summarized in Table 2 for reference.

**Table 2.** IR band positions and corresponding species based on previous reports.

Positions ( $\text{cm}^{-1}$ )	Species	References
1617	$\sigma_{as}(\text{NH}_3)$ on Lewis acid centers	[18,19,33]
1465, 1496	$\sigma_{as}(\text{NH}_4^+)$ on Brønsted acid centers	[33,34]
3182	$\text{NH}_3$ -Cu species	[18,35]
3221, 3347	$\text{NH}_4^+$ species	[19,36]
3736, 3630, 3540	Bridged hydroxyl Al-OH-Si	[37,38]

Figure 6 shows the  $\text{NH}_3$  adsorption DRIFTS spectra on 5Cu-USY and 5Cu8Ce-USY catalysts before/after hydrothermal ageing. Once  $\text{NH}_3$  was introduced into the reaction chamber, two distinct IR bands could be seen at  $1617 \text{ cm}^{-1}$  and  $1465 \text{ cm}^{-1}$ ; the former was ascribed to the asymmetric vibration of molecularly adsorbed ammonia on Lewis acid centers ( $\sigma_{as}(\text{NH}_3)$ ), while the latter was assigned to the asymmetric vibration of  $\text{NH}_4^+$

adsorbed on the Brønsted acid centers ( $\sigma_{as}(\text{NH}_4^+)$ ). Also, three major IR bands could be observed at  $3182\text{ cm}^{-1}$ ,  $3221\text{ cm}^{-1}$ , and  $3347\text{ cm}^{-1}$ ; whereas the  $3182\text{ cm}^{-1}$  band was related to N–H stretching vibrations of  $\text{NH}_3$  adsorbed on cationic Cu sites, the  $3221\text{ cm}^{-1}$  and  $3347\text{ cm}^{-1}$  bands were attributed to  $\text{NH}_4^+$  groups. Moreover, three negative bands appeared at  $3736\text{ cm}^{-1}$ ,  $3630\text{ cm}^{-1}$ , and  $3547\text{ cm}^{-1}$ , which were generated due to the consumption of surface hydroxyl sites by  $\text{NH}_3$ , reducing the corresponding OH stretching vibrations. Brønsted acid centers and Lewis acid centers were saturated with  $\text{NH}_3$  after 20 min adsorption. Upon Ar purging for 30 min after  $\text{NH}_3$  saturated adsorption, the intensity of each IR band was weakened slightly, indicating relatively stable adsorption of  $\text{NH}_3$  on surface acid centers. After hydrothermal ageing, the intensity of  $\text{NH}_3$  adsorbed on Lewis acid centers ( $1617\text{ cm}^{-1}$  band) gradually increased, which could be related to partial dealumination of the zeolite frameworks during hydrothermal ageing. On the other hand, the intensity of  $\text{NH}_4^+$  adsorbed on the Brønsted acid centers ( $1465\text{ cm}^{-1}$  band) dropped significantly, suggesting severe loss of Brønsted acid centers due to loss of surface hydroxy groups. By comparing 5Cu-USY-700H and 5Cu8Ce-USY-700H, we can see that Ce doping could not attenuate the loss of either Brønsted acid centers or Lewis acid centers on the catalyst's surface during hydrothermal ageing.

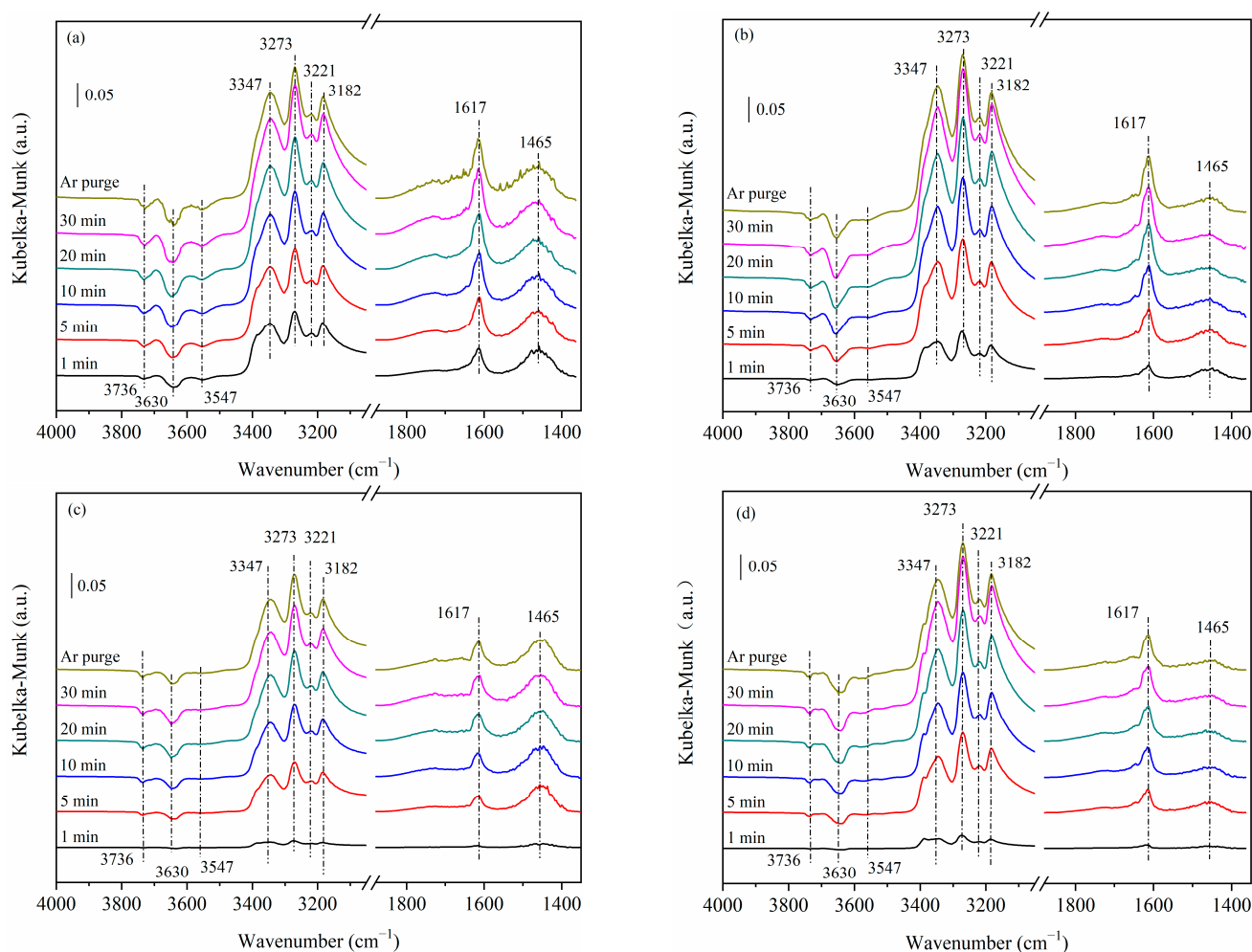


**Figure 6.** DRIFTS spectra of  $\text{NH}_3$  adsorption on 5Cu-USY and 5Cu8Ce-USY catalysts before/after hydrothermal ageing: 5Cu-USY (a), 5Cu-USY-700H (b), 5CuCe-USY (c), and 5Cu8Ce-USY-700H (d).

Figure 7 shows DRIFTS spectra of the “ $\text{NO} + \text{O}_2$ ” reaction after  $\text{NH}_3$  saturated adsorption on 5Cu-USY and 5Cu8Ce-USY catalysts before/after hydrothermal ageing. When the “ $\text{NO} + \text{O}_2$ ” reaction atomsphere was introduced into the reaction chamber, the  $1617\text{ cm}^{-1}$

band representing  $\text{NH}_3$  adsorbed on Lewis acid centers exhibited an obvious decrease, along with similar decreasing negative OH bands ( $3736\text{ cm}^{-1}$ ,  $3630\text{ cm}^{-1}$ , and  $3540\text{ cm}^{-1}$ ). This demonstrates clear consumption of surface-adsorbed  $\text{NH}_3$ . Compared to the fresh 5Cu-USY catalyst, the above IR bands disappeared more rapidly on the 5Cu-USY-700H sample after hydrothermal ageing, which reflects its better low-temperature SCR activity. Moreover, the IR bands around  $1465\text{ cm}^{-1}$  first increased and then started to descend with a broadened range, around  $1440$  to  $1500\text{ cm}^{-1}$ . Considering no more  $\text{NH}_3$  was fed into the reaction atmosphere, the intensity elevation of  $1465\text{ cm}^{-1}$  bands could be explained due to formation of surface nitrates ( $\text{NH}_4\text{NO}_3$ ) or nitrites ( $\text{NH}_4\text{NO}_2$ ) species on the Brønsted acid centers, which present various IR bands within  $1440$ – $1630\text{ cm}^{-1}$  ranges. As the reaction continued to proceed, these nitrates/nitrite species further participated in the SCR reaction and eventually decomposed; thus, the corresponding IR bands first increased and then decreased. For the Ce-doped catalyst, similar IR band evolution trends could be observed on the fresh 5Cu8Ce-USY catalyst. However, for 5Cu8Ce-USY-700H after hydrothermal ageing, the  $1465\text{ cm}^{-1}$  bands disappeared remarkably fast with time evolving, which could be caused by the accelerated nitrates/nitrite oxidation due to the enhanced redox ability of  $\text{CuO}_x$ – $\text{CeO}_2$  interaction.

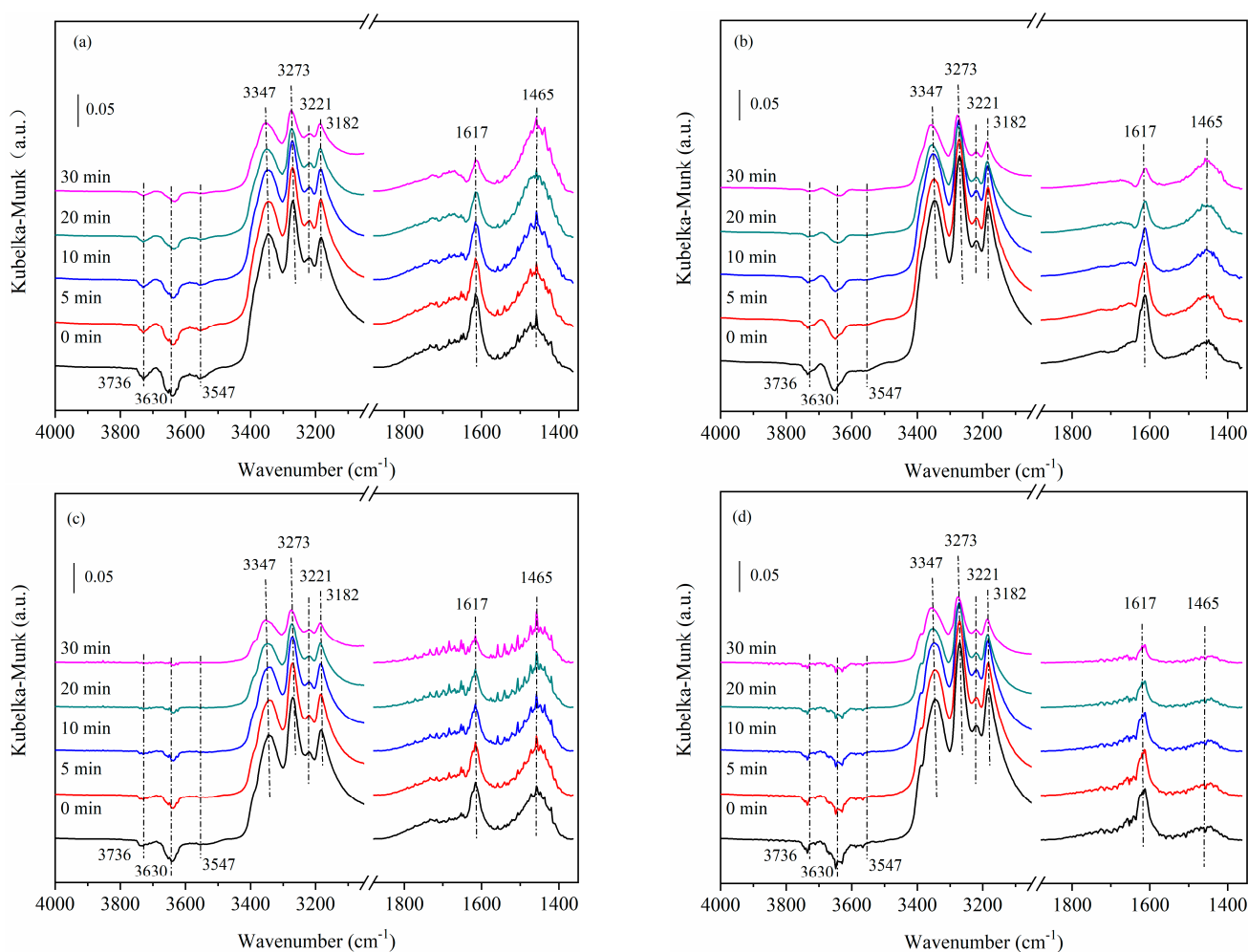


**Figure 7.** DRIFTS spectra of  $\text{NO} + \text{O}_2$  reaction after  $\text{NH}_3$  adsorption on 5Cu-USY and 5Cu8Ce-USY catalysts before/after hydrothermal ageing: 5Cu-USY (a), 5Cu-USY-700H (b), 5CuCe-USY (c), and 5Cu8Ce-USY-700H (d).

### 2.7. Brief Discussions about the Structure–Activity Correlations

Different Cu species have been previously demonstrated to exist in the Cu-USY catalysts, for example, highly dispersed  $\text{CuO}_x$  species,  $\text{Cu}^{2+}/\text{Cu}^+$  species located in the sodalite cavities, and  $\text{Cu}^{2+}/\text{Cu}^+$  species entering the super cages of USY zeolites. The  $\text{CuO}_x$  species are generally considered as oxidation centers during the SCR reaction, and they could also accelerate  $\text{NH}_3$  oxidation at high temperatures [34]. For the isolated  $\text{Cu}^{2+}/\text{Cu}^+$  species, both  $\text{Cu}^{2+}$  and  $\text{Cu}^+$  cations play important roles in the low-temperature SCR reaction process via the reversible redox cycle " $\text{Cu}^{2+} \leftrightarrow \text{Cu}^+$ ". Hence, the different coordination environment of Cu species should be more worthy of attention than the chemical valent states [19,39]. The three most populated Cu cationic sites could be identified based on previous reports (site I, site II, and site III in Figure 8) [19,40,41]. Site I was located in the hexagonal prism deviating from the face of the d6r subunits, and site II was set in the sodalite cavities near the six-membered ring, while site III was present near four-membered rings facing the super cages of the zeolite structures. The Cu cations at site I could not be reached by reactant molecules such as  $\text{NO}/\text{NH}_3$  due to the limited dimensions of the small windows connecting the sodalite cavities and hexagonal prism. For the Cu cations at site II, although they were accessible by reactant molecules, these Cu cations have been reported to be highly mobile and tend to migrate into the super cages, losing coordination with the lattice oxygen. Therefore, these Cu species at site II contribute in quite a limited manner to the SCR reactivity. As for the Cu species at site III in the super cages, they can be highly interactive with the reactant molecules due to the large diameter of the super cage windows (about 7.4 Å), while simultaneously maintaining coordination with the lattice oxygen to proceed with the " $\text{Cu}^{2+} \leftrightarrow \text{Cu}^+$ " redox cycle during the reaction. Thus, Cu species at site III in the super cages are widely recognized as essential active sites for the low-temperature  $\text{NH}_3$ -SCR reaction, but they could also cause an  $\text{NH}_3$  oxidation problem with excessive content [19,22,23,42]. For 5Cu-USY, the isolated  $\text{Cu}^+$  species in the sodalite cavities migrated towards the super cages of the USY zeolites during hydrothermal ageing, and the increased content of Cu species at site III was beneficial for the low-temperature activity improvement while simultaneously facilitating  $\text{NO}_2/\text{N}_2\text{O}$  at high temperatures. For 5Cu8Ce-USY, Ce doping of Cu-USY could cause the internal cages to be pre-occupied by the Ce cations and thereby inhibit Cu species migration. Additionally, the content of highly dispersed  $\text{CuO}_x$  species was also increased due to the  $\text{CuO}_x$ – $\text{CeO}_2$  strong interaction. These  $\text{CuO}_x$  species could promote further oxidative decomposition of nitrate/nitrite intermediates and improve the catalytic performance [43–45]. But, at the same time, they also caused more serious byproduct formation.

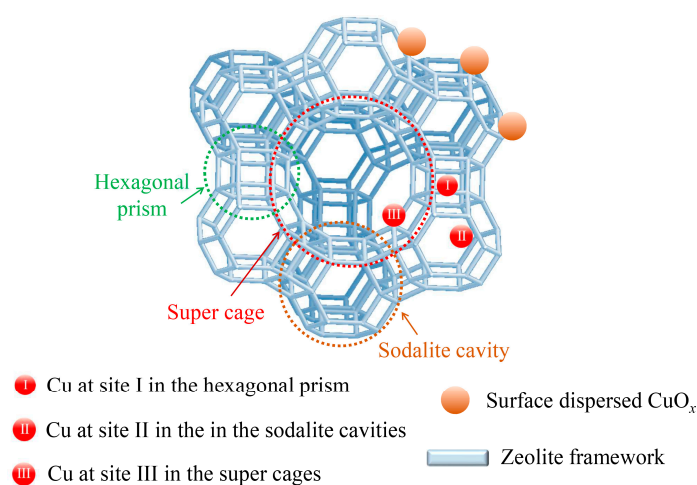


**Figure 8.** Possible Cu species and their sites in the Cu-USY catalysts.

For the reaction mechanism, it is generally agreed that the SCR reaction over the Cu-USY catalyst follows the Eley–Rideal mechanism; the gas phase  $\text{NH}_3$  was first adsorbed

on the catalyst's surface to form ligand-state  $\text{NH}_3$ , which was then oxidatively activated to form the  $-\text{NH}_2$  group and reacted with gaseous  $\text{NO}$  to generate  $\text{NH}_2\text{NO}$  intermediate species; and the  $\text{NH}_2\text{NO}$  intermediate finally decomposed into  $\text{N}_2$  and  $\text{H}_2\text{O}$ . For the Ce-doped CuCe-USY catalysts, considering the significantly enhanced redox ability of CuCe-USY by Ce doping,  $\text{NO}$  could be more easily oxidized into  $\text{NO}_2$ , and, hence, the Langmuir–Hinshelwood mechanism could also occur over CuCe-USY; the gaseous  $\text{NO}$  was first adsorbed on the catalyst's surface and then oxidized to form either the adsorbed  $\text{NO}_2$  or the nitrates/nitrite species. These  $\text{NO}_2/-\text{NO}_2$  species rapidly reacted with the  $\text{NH}_4^+$  species formed via  $\text{NH}_3$  adsorbed on the Brønsted acid centers to ultimately generate  $\text{N}_2$  and  $\text{H}_2\text{O}$ . Therefore, multiple reaction pathways may exist for the low-temperature  $\text{NH}_3$ -SCR reaction over CuCe-USY catalysts.

### 3. Experimental Section

#### 3.1. Catalysts Preparation

A Cu-USY catalyst was prepared via conventional co-impregnation method (Figure S1). First, a quantitative amount of  $\text{Cu}(\text{NO}_3)_2$  (Analytical Reagent, Sinopharm Chemical Reagent Co., Ltd., Beijing, China) was dissolved in deionized water to obtain the metal precursor solution. H-USY zeolites ( $\text{SiO}_2/\text{Al}_2\text{O}_3$  molar ratio = 5.2, Analytical Reagent, NKF-8, Nankai University Catalyst Co., Ltd., Tianjin, China) were added into the above solution under vigorous stirring at  $80^\circ\text{C}$  for 3 h. The impregnated sample was then dried at  $100^\circ\text{C}$  for 2 h and calcined at  $500^\circ\text{C}$  in air for 5 h. The obtained Cu-USY catalyst was denoted as “5Cu-USY”; namely, the Cu loading content was 5 wt.% (the actual Cu content was determined by ICP-AES as 4.93 wt.%).

The Ce-doped CuCe-USY catalyst was prepared via similar co-impregnation method using both  $\text{Cu}(\text{NO}_3)_2$  and  $\text{Ce}(\text{NO}_3)_3$  (Analytical Reagent, Sinopharm Chemical Reagent Co., Ltd., Beijing, China) as metal precursors. The obtained CuCe-USY catalyst was denoted as “5Cu8Ce-USY”; namely, the Cu loading content was also 5 wt.%, while the Ce doping content was 8 wt.% (the actual Cu and Ce contents were determined by ICP-AES as 4.96 wt.% and 7.92 wt.%). Such Cu and Ce contents were chosen based on the optimized CuCe-USY catalyst compositions in our previous studies [18,19].

#### 3.2. Hydrothermal Ageing

The obtained 5Cu-USY and 5Cu8Ce-USY catalysts were subjected to hydrothermal ageing for 4 h under air/steam vapor flow containing 10 vol.%  $\text{H}_2\text{O}$ . The ageing temperatures were set at  $700^\circ\text{C}$ . The aged catalysts were labelled using “–700H” as a suffix (H stands for hydrothermal ageing, and the number 700 stands for the ageing temperature).

#### 3.3. Catalyst Characterization

X-ray diffraction (XRD) analysis was performed on a Shimadzu XRD7000 X-ray diffractometer (Shimadzu Corporation, Kyoto, Japan) equipped with monochromate Cu  $\text{K}\alpha$  radiation operating at 40 kV tube voltage and 30 mA tube current. The XRD diffractograms were collected from  $5$  to  $50^\circ$  with a scanning rate of  $5^\circ/\text{min}$ , and the crystalline phases were identified using standard JCPDS cards.

$\text{H}_2$  temperature-programmed reduction ( $\text{H}_2$ -TPR) tests were conducted in the Chem-BET PULSAR chemisorption apparatus (Quantachrome Instruments, Boynton Beach, FL, USA). A 100 mg sample was purged by Ar flow at  $400^\circ\text{C}$  for 30 min before tests and then cooled down to  $50^\circ\text{C}$ . Then, 5 vol.%  $\text{H}_2/\text{Ar}$  flow (40 mL/min) was introduced into the reactor until the baseline was stable. The  $\text{H}_2$ -TPR profiles were recorded by monitoring  $\text{H}_2$  consumption using thermal conductivity detector (TCD) signals while simultaneously raising the reactor temperature to  $600^\circ\text{C}$  (heating rate of  $10^\circ\text{C}/\text{min}$ ).

X-ray photoelectron spectroscopy (XPS) analysis was performed on a Thermo ESCALAB 250 X-ray photoelectron spectrometer (Thermo Fisher Scientific, Waltham, MA, USA) equipped with mono-chromated Al  $\text{K}\alpha$  radiation. The binding energies were calibrated using the C 1 s peak at 284.8 eV.

CO chemisorption diffuse reflectance infrared Fourier-transform spectroscopy (CO DRIFTS) tests were conducted on the Nicolet 6700 Fourier transform infrared spectrometer (Thermo Fisher Scientific, Waltham, MA, USA) equipped with low-temperature mercury cadmium telluride (MCT) detector. The 100 mg catalyst was first pretreated in Ar at 400 °C for 0.5 h. After cooling down to RT, 0.5 vol.% CO/Ar mixed gas was introduced into the reaction chamber until CO adsorption was saturated. CO DRIFTS spectra were collected by accumulating 32 scans at 4 cm<sup>−1</sup> resolution.

The in situ diffuse reflectance infrared Fourier-transform spectroscopy (in situ DRIFTS) experiments were performed on the same Nicolet 6700 Fourier transform infrared spectrometer (Thermo Fisher Scientific, Waltham, MA, USA). The 100 mg catalyst was firstly pretreated in 5 vol.% O<sub>2</sub>/Ar at 400 °C for 30 min and then cooled down to 200 °C. During the DRIFTS tests, 1000 ppm NH<sub>3</sub>/Ar was injected into the cell for 30 min adsorption first and purged with Ar, then 1000 ppm NO, along with 5 vol.% O<sub>2</sub>, was introduced as reaction gas. The background spectra were collected at different temperatures before injecting the reaction gases. DRIFTS spectra were collected by accumulating 32 scans at 4 cm<sup>−1</sup> resolutions with different time intervals.

### 3.4. Catalytic Activity Tests

The NH<sub>3</sub>-SCR activity tests were carried out in a fixed-bed reactor. The reaction gas contained 500 ppm NO, 500 ppm NH<sub>3</sub>, 5 vol.% O<sub>2</sub>, and Ar as balancing gas. The total gas hourly space velocity (GHSV) of inlet gas was set at 48,000 h<sup>−1</sup>. During the activity test, the reactor temperature was raised to certain points and maintained until the reaction was stable. The concentrations of NO, NH<sub>3</sub>, NO<sub>2</sub>, and N<sub>2</sub>O in the outlet gases were quantitatively analyzed using a Bruker EQUINOX 55 FTIR spectrometer (Bruker Corporation, Billerica, MA, USA) equipped with a multiple-reflection gas cell (cell volume 1.33 L, path length 10.0 m) and a pre-installed quantitative gas analysis program. NO and NH<sub>3</sub> conversions were calculated according to the following formulas:

$$C_{NO} = \frac{NO_{inlet} - NO_{outlet}}{NO_{inlet}} \times 100\% \quad (1)$$

$$C_{NH_3} = \frac{NH_{3-inlet} - NH_{3-outlet}}{NH_{3-inlet}} \times 100\% \quad (2)$$

where  $C_{NO}$  (%) and  $C_{NH_3}$  (%) are the conversion of NO and NH<sub>3</sub>, respectively;  $NO_{inlet}$  (ppm) and  $NO_{outlet}$  (ppm) are the NO concentration before and after the SCR activity test, respectively;  $NH_{3-inlet}$  (ppm) and  $NH_{3-outlet}$  (ppm) are the NH<sub>3</sub> concentration before and after the SCR activity test, respectively.

## 4. Conclusions

In this study, Cu-USY and Ce-doped CuCe-USY zeolite catalysts were prepared using impregnation method and subjected to high-temperature hydrothermal ageing. The catalytic performance for NH<sub>3</sub>-SCR was evaluated, and detailed characterizations were conducted to explore the possible structure–activity correlations. Results showed that, for the 5Cu-USY catalyst, hydrothermal ageing caused the isolated Cu<sup>+</sup> species in the sodalite cavities to migrate towards the super cages of the USY zeolites. The increased content of Cu<sup>+</sup> species in the super cages was conducive to improving the low-temperature SCR activity, but it also promoted ammonia oxidation to generate unfavorable NO<sub>2</sub> and N<sub>2</sub>O at high temperatures. Ce doping can restrain Cu species' migration during hydrothermal ageing by self-occupying the internal cage sites. It can also increase the surface active oxygen concentration by establishing a CuO<sub>x</sub>–CeO<sub>2</sub> strong interaction, which helps to promote lattice oxygen mobility by forming more oxygen vacancies. Therefore, the effect of Ce doping is like two sides of the same coin. On the one hand, it can accelerate oxidative decomposition of nitrate/nitrite intermediates and improve the catalytic performance; on the other hand, it also causes the severe generation of byproducts NO<sub>2</sub> and N<sub>2</sub>O.

**Supplementary Materials:** The following supporting information can be downloaded at: <https://www.mdpi.com/article/10.3390/catal13121485/s1>, Figure S1: Synthesis scheme of the 5Cu-USY catalysts; Table S1: Comparison of the NH<sub>3</sub>-SCR activity of fresh catalysts in this work with other reports; Table S2: Peak areas and relative proportion of each peak in the H<sub>2</sub>-TPR profiles.

**Author Contributions:** Conceptualization, Q.S. (Qi Sun), H.Y., J.W. and R.Z.; methodology, H.Y., W.H. and X.W.; validation, H.Y., J.W., Y.L. and R.Z.; investigation, H.Y., Y.L. and X.W.; resources, C.S., Q.S. (Qingai Shi) and G.W.; data curation, H.Y., C.S., Q.S. (Qingai Shi) and Y.L.; writing—original draft preparation, Q.S. (Qi Sun) and J.W.; writing—review and editing, J.W., G.W. and R.Z.; visualization, Q.S. (Qi Sun), W.H. and X.W.; supervision, R.Z.; project administration, R.Z.; funding acquisition, Q.S. (Qi Sun), J.W., G.W. and R.Z. All authors have read and agreed to the published version of the manuscript.

**Funding:** This work was supported by the National Key Research and Development Program of China (2022YFB3504200), the Jiangsu Province Science and Technology Plan Special Fund (BZ2022053), Key Research and Development Program of Anhui Province (202104g01020006), the Natural Science Foundation of Jiangsu Province (BK20201037), the Scientific Research Fund of Nanjing Institute of Technology (nos. YKJ2019111 and YKJ2019110), the Students' Science and Technology Innovation Fund of Nanjing Institute of Technology (TB202312034), and the provincial key project of the Innovation and Entrepreneurship Training Program for College Students in Jiangsu Province (202311276007Z).

**Data Availability Statement:** Data will be available on request.

**Conflicts of Interest:** The authors declare no conflict of interest.

## References

- Joshi, A. Review of vehicle engine efficiency and emissions. *SAE Int. J. Adv. Curr. Prac. Mobil.* **2019**, *1*, 734–761. [\[CrossRef\]](#)
- Qu, Y.; An, J.; He, Y.; Zheng, J. An overview of emissions of SO<sub>2</sub> and NO<sub>x</sub> and the long-range transport of oxidized sulfur and nitrogen pollutants in East Asia. *J. Environ. Sci.* **2016**, *44*, 13–25. [\[CrossRef\]](#)
- Shelef, M.; McCabe, R.W. Twenty-five years after introduction of automotive catalysts: What next? *Catal. Today* **2020**, *62*, 35–50. [\[CrossRef\]](#)
- Topsøe, N.Y. Mechanism of the selective catalytic reduction of nitric oxide by ammonia elucidated by in situ on-line Fourier transform infrared spectroscopy. *Science* **1994**, *265*, 1217–1219. [\[CrossRef\]](#)
- Zhang, Q.J.; Wu, Y.F.; Yuan, H.R. Recycling strategies of spent V<sub>2</sub>O<sub>5</sub>-WO<sub>3</sub>/TiO<sub>2</sub> catalyst: A review. *Resour. Conserv. Recycl.* **2020**, *161*, 104983. [\[CrossRef\]](#)
- Szymaszek, A.; Samojeden, B.; Motak, M. The deactivation of industrial SCR catalysts—A short review. *Energies* **2020**, *13*, 3870. [\[CrossRef\]](#)
- Andana, T.; Rappe, K.G.; Gao, F.; Szanyi, J.; Pereira-Hernandez, X.; Wang, Y. Recent advances in hybrid metal oxide–zeolite catalysts for low-temperature selective catalytic reduction of NO<sub>x</sub> by ammonia. *Appl. Catal. B Environ.* **2021**, *291*, 120054. [\[CrossRef\]](#)
- Pu, Y.; Xie, X.; Jiang, W.; Yang, L.; Jiang, X.; Yao, L. Low-temperature selective catalytic reduction of NO<sub>x</sub> with NH<sub>3</sub> over zeolite catalysts: A review. *Chin. Chem. Lett.* **2020**, *31*, 2549–2555. [\[CrossRef\]](#)
- Grossale, A.; Nova, I.; Tronconi, E. Study of a Fe–zeolite-based system as NH<sub>3</sub>-SCR catalyst for diesel exhaust aftertreatment. *Catal. Today* **2008**, *136*, 18–27. [\[CrossRef\]](#)
- Ellmers, I.; Vélez, R.P.; Bentrup, U.; Brückner, A.; Grünert, W. Oxidation and selective reduction of NO over Fe-ZSM-5—How related are these reactions? *J. Catal.* **2014**, *311*, 199–211. [\[CrossRef\]](#)
- Ma, Y.; Liu, Y.; Li, Z.; Geng, C.; Bai, X.; Cao, D. Synthesis of CuCe co-modified mesoporous ZSM-5 zeolite for the selective catalytic reduction of NO by NH<sub>3</sub>. *Environ. Sci. Pollut. Res.* **2020**, *27*, 9935–9942. [\[CrossRef\]](#) [\[PubMed\]](#)
- Mohan, S.; Dinesha, P.; Kumar, S. NO<sub>x</sub> reduction behaviour in copper zeolite catalysts for ammonia SCR systems: A review. *Chem. Eng. J.* **2020**, *384*, 123253. [\[CrossRef\]](#)
- Tarach, K.A.; Jabłońska, M.; Pyra, K.; Liebau, M.; Reiprich, B.; Gläser, R.; Góra-Marek, K. Effect of zeolite topology on NH<sub>3</sub>-SCR activity and stability of Cu-exchanged zeolites. *Appl. Catal. B Environ.* **2021**, *284*, 119752. [\[CrossRef\]](#)
- Liu, B.; Yao, D.; Wu, F.; Wei, L.; Li, X.; Wang, X. Experimental investigation on N<sub>2</sub>O formation during the selective catalytic reduction of NO<sub>x</sub> with NH<sub>3</sub> over Cu-SSZ-13. *Ind. Eng. Chem. Res.* **2019**, *58*, 20516–20527. [\[CrossRef\]](#)
- Zones, S.I.; Van Nordstrand, R.A. Novel zeolite transformations: The template-mediated conversion of Cubic P zeolite to SSZ-13. *Zeolites* **1988**, *8*, 166–174. [\[CrossRef\]](#)
- Wan, J.; Chen, J.; Zhao, R.; Zhou, R. One-pot synthesis of Fe/Cu-SSZ-13 catalyst and its highly efficient performance for the selective catalytic reduction of nitrogen oxide with ammonia. *J. Environ. Sci.* **2021**, *100*, 306–316. [\[CrossRef\]](#)
- Ochońska, J.; McClymont, D.; Jodłowski, P.J.; Knapik, A.; Gil, B.; Makowski, W.; Łasocha, W.; Kołodziej, A.; Kolaczowski, S.T.; Łojewska, J. Copper exchanged ultrastable zeolite Y—A catalyst for NH<sub>3</sub>-SCR of NO<sub>x</sub> from stationary biogas engines. *Catal. Today* **2012**, *191*, 6–11. [\[CrossRef\]](#)

18. Zhou, J.; Zhao, C.; Lin, J.; Yang, H.; Zhou, R. Promotional effects of cerium modification of Cu-USY catalysts on the low-temperature activity of NH<sub>3</sub>-SCR. *Catal. Commun.* **2018**, *114*, 60–64. [\[CrossRef\]](#)
19. Wan, J.; Yang, H.; Shi, Y.; Liu, Y.; Zhang, J.; Zhang, J.; Wu, G.; Zhou, R. Effect of Cu loading content on the catalytic performance of Cu-USY catalysts for selective catalytic reduction of NO with NH<sub>3</sub>. *J. Environ. Sci.* **2023**, *126*, 445–458. [\[CrossRef\]](#)
20. Kwak, J.H.; Tran, D.; Burton, S.D.; Szanyi, J.; Lee, J.H.; Peden, C.H. Effects of hydrothermal aging on NH<sub>3</sub>-SCR reaction over Cu/zeolites. *J. Catal.* **2021**, *287*, 203–209. [\[CrossRef\]](#)
21. Martinez-Ortigosa, J.; Lopes, C.W.; Agostini, G.; Palomares, A.E.; Blasco, T.; Rey, F. AgY zeolite as catalyst for the selective catalytic oxidation of NH<sub>3</sub>. *Microporous Mesoporous Mater.* **2021**, *323*, 111230. [\[CrossRef\]](#)
22. Delahay, G.; Kieger, S.; Tanchoux, N.; Trens, P.; Coq, B. Kinetics of the selective catalytic reduction of NO by NH<sub>3</sub> on a Cu-faujasite catalyst. *Appl. Catal. B Environ.* **2004**, *52*, 251–257. [\[CrossRef\]](#)
23. Kieger, S.; Delahay, G.; Coq, B.; Neveu, B. Selective catalytic reduction of nitric oxide by ammonia over Cu-FAU catalysts in oxygen-rich atmosphere. *J. Catal.* **1999**, *183*, 267–280. [\[CrossRef\]](#)
24. Dang, T.T.H.; Zubowa, H.L.; Bentrup, U.; Richter, M.; Martin, A. Microwave-assisted synthesis and characterization of Cu-containing AlPO<sub>4</sub>-5 and SAPO-5. *Microporous Mesoporous Mat.* **2009**, *123*, 209–220. [\[CrossRef\]](#)
25. Song, L.; Zhan, Z.; Liu, X.; He, H.; Qiu, W.; Zi, X. NO<sub>x</sub> selective catalytic reduction by ammonia over Cu-ETS-10 catalysts. *Chin. J. Catal.* **2014**, *35*, 1030–1035. [\[CrossRef\]](#)
26. Kwak, J.H.; Zhu, H.Y.; Lee, J.H.; Peden, C.H.; Szanyi, J. Two different cationic positions in Cu-SSZ-13? *Chem. Commun.* **2012**, *48*, 4758–4760. [\[CrossRef\]](#)
27. Wan, J.; Chen, J.; Shi, Y.; Wang, Y.; Liu, Y.; Zhang, J.; Wu, G.; Zhou, R. In-situ one-pot synthesis of Ti/Cu-SSZ-13 catalysts with highly efficient NH<sub>3</sub>-SCR catalytic performance as well as superior H<sub>2</sub>O/SO<sub>2</sub> tolerability. *Catal. Surv. Asia* **2022**, *26*, 346–357. [\[CrossRef\]](#)
28. Han, S.; Cheng, J.; Zheng, C.; Ye, Q.; Cheng, S.; Kang, T.; Dai, H. Effect of Si/Al ratio on catalytic performance of hydrothermally aged Cu-SSZ-13 for the NH<sub>3</sub>-SCR of NO in simulated diesel exhaust. *Appl. Surf. Sci.* **2017**, *419*, 382–392. [\[CrossRef\]](#)
29. Wang, H.; Luo, S.; Zhang, M.; Liu, W.; Wu, X.; Liu, S. Roles of oxygen vacancy and O<sup>x−</sup> in oxidation reactions over CeO<sub>2</sub> and Ag/CeO<sub>2</sub> nanorod model catalysts. *J. Catal.* **2018**, *368*, 365–378. [\[CrossRef\]](#)
30. Zhao, L.; Zhang, Z.; Li, Y.; Leng, X.; Zhang, T.; Yuan, F.; Niu, X.; Zhu, Y. Synthesis of Ce<sub>a</sub>MnO<sub>x</sub> hollow microsphere with hierarchical structure and its excellent catalytic performance for toluene combustion. *Appl. Catal. B Environ.* **2019**, *245*, 502–512. [\[CrossRef\]](#)
31. Atribak, I.; Bueno-López, A.; García-García, A. Role of yttrium loading in the physico-chemical properties and soot combustion activity of ceria and ceria–zirconia catalysts. *J. Mol. Catal. A Chem.* **2009**, *300*, 103–110. [\[CrossRef\]](#)
32. Lambrou, P.S.; Efstathiou, A.M. The effects of Fe on the oxygen storage and release properties of model Pd–Rh/CeO<sub>2</sub>–Al<sub>2</sub>O<sub>3</sub> three-way catalyst. *J. Catal.* **2006**, *240*, 182–193. [\[CrossRef\]](#)
33. Martins, G.V.A.; Berlier, G.; Bisio, C.; Coluccia, S.; Pastore, H.O.; Marchese, L. Quantification of Brønsted acid sites in microporous catalysts by a combined FTIR and NH<sub>3</sub>-TPD study. *J. Phys. Chem. C* **2008**, *112*, 7193–7200. [\[CrossRef\]](#)
34. Wang, L.; Li, W.; Qi, G.S.; Weng, D. Location and nature of Cu species in Cu/SAPO-34 for selective catalytic reduction of NO with NH<sub>3</sub>. *J. Catal.* **2012**, *289*, 21–29. [\[CrossRef\]](#)
35. Sjövall, H.; Fridell, E.; Blint, R.J.; Olsson, L. Identification of adsorbed species on Cu-ZSM-5 under NH<sub>3</sub> SCR conditions. *Top. Catal.* **2007**, *42*, 113–117. [\[CrossRef\]](#)
36. Wang, L.; Li, W.; Schmieg, S.J.; Weng, D. Role of Brønsted acidity in NH<sub>3</sub> selective catalytic reduction reaction on Cu/SAPO-34 catalysts. *J. Catal.* **2015**, *324*, 98–106. [\[CrossRef\]](#)
37. Rivallan, M.; Ricchiardi, G.; Bordiga, S.; Zecchina, A. Adsorption and reactivity of nitrogen oxides (NO<sub>2</sub>, NO, N<sub>2</sub>O) on Fe–zeolites. *J. Catal.* **2009**, *264*, 104–116. [\[CrossRef\]](#)
38. Onida, B.; Gabelica, Z.; Lourenco, J.; Garrone, E. Spectroscopic characterization of hydroxyl groups in SAPO-40. 1. Study of the template-free samples and their interaction with ammonia. *J. Phys. Chem.* **1996**, *100*, 11072–11079. [\[CrossRef\]](#)
39. Ikuno, T.; Grundner, S.; Jentys, A.; Li, G.N.; Pidko, E.; Fulton, J.; Sanchez-Sanchez, M.; Lercher, J.A. Formation of active Cu-oxo clusters for methane oxidation in Cu-exchanged mordenite. *J. Phys. Chem. C* **2019**, *123*, 8759–8769. [\[CrossRef\]](#)
40. Deka, U.; Lezcano-Gonzalez, I.; Weckhuysen, B.M.; Beale, A.M. Local environment and nature of Cu active sites in zeolite-based catalysts for the selective catalytic reduction of NO<sub>x</sub>. *ACS Catal.* **2013**, *3*, 413–427. [\[CrossRef\]](#)
41. Seo, S.M.; Lim, W.T.; Seff, K. Crystallographic verification that copper (II) coordinates to four of the oxygen atoms of zeolite 6-rings. Two single-crystal structures of fully dehydrated, largely Cu<sup>2+</sup>-exchanged zeolite Y (FAU, Si/Al = 1.56). *J. Phys. Chem. C* **2012**, *116*, 963–974. [\[CrossRef\]](#)
42. Garnier, T.; Danel, M.; Magné, V.; Pujol, A.; Bénétteau, V.; Pale, P.; Chassaing, S. Copper (I)–USY as a ligand-free and recyclable catalyst for ullmann-type O-, N-, S-, and C-arylation reactions: Scope and application to total synthesis. *J. Org. Chem.* **2018**, *83*, 6408–6422. [\[CrossRef\]](#) [\[PubMed\]](#)
43. Lin, Q.; Li, J.; Ma, L.; Hao, J. Selective catalytic reduction of NO with NH<sub>3</sub> over Mn–Fe/USY under lean burn conditions. *Catal. Today* **2010**, *151*, 251–256. [\[CrossRef\]](#)

44. Xie, Q.; Jin, Q.; Ye, Y.; Hou, S.; Wang, X.; He, F. Effect of La/Ce modification over Cu based Y zeolite catalysts on high temperature selectivity for selective catalytic reduction with ammonia. *J. Clean. Prod.* **2022**, *362*, 132255. [[CrossRef](#)]
45. Jodłowski, P.J.; Czekaj, I.; Stachurska, P.; Kuterasiński, Ł.; Chmielarz, L.; Jędrzejczyk, R.J.; Jeleń, P.; Sitarz, M.; Górecka, S.; Mazur, M.; et al. Experimental and theoretical studies of sonically prepared Cu–Y, Cu–USY and Cu–ZSM-5 catalysts for SCR deNO<sub>x</sub>. *Catalysts* **2021**, *11*, 824. [[CrossRef](#)]

**Disclaimer/Publisher’s Note:** The statements, opinions and data contained in all publications are solely those of the individual author(s) and contributor(s) and not of MDPI and/or the editor(s). MDPI and/or the editor(s) disclaim responsibility for any injury to people or property resulting from any ideas, methods, instructions or products referred to in the content.